Supplementary Information for Polarization switching and electrical control of interlayer excitons in two-dimensional van der Waals heterostructures

Alberto Ciarrocchi[1,2†], Dmitrii Unuchek[1,2†], Ahmet Avsar[1,2], Kenji Watanabe[3], Takashi Taniguchi[3], Andras Kis[1,2*]

[1]Electrical Engineering Institute, École Polytechnique Fédérale de Lausanne (EPFL), CH-1015 Lausanne, Switzerland
[2]Institute of Materials Science and Engineering, École Polytechnique Fédérale de Lausanne (EPFL), CH-1015 Lausanne, Switzerland
[3]National Institute for Materials Science, 1-1 Namiki, Tsukuba 305-0044, Japan

[†]*These authors contributed equally*
[*]*Correspondence should be addressed to: Andras Kis, andras.kis@epfl.ch*

1. Monolayer PL spectra

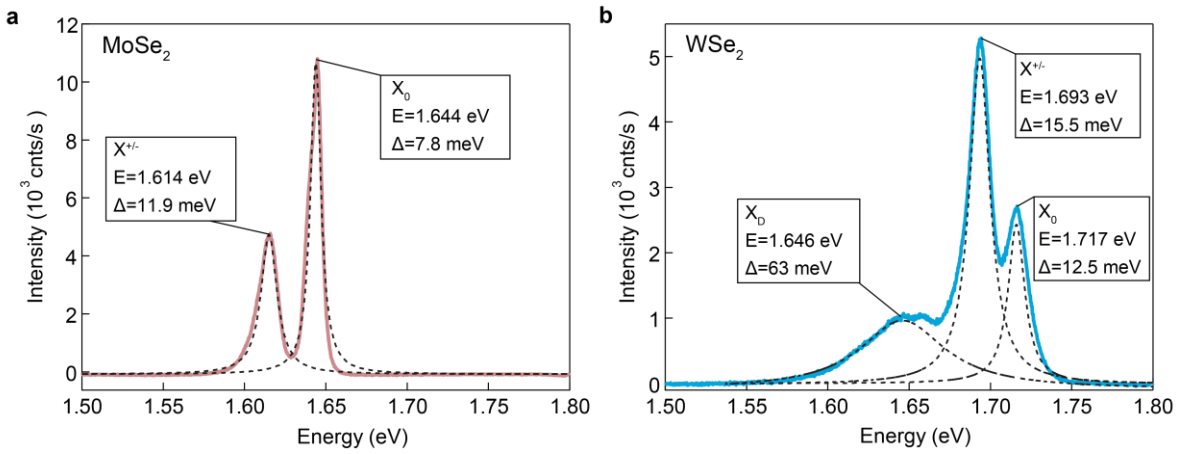

Supplementary Figure S1. PL from individual monolayers. a, PL spectrum from monolayer $MoSe_2$ and **b**, PL spectrum from monolayer WSe_2 together with Lorentzian fitting of the emission peaks. X_0, $X^{+/-}$ and X_D are neutral, charged and defect-bounded excitons respectively.

2. Spatial maps of intra- and inter-layer excitonic emission

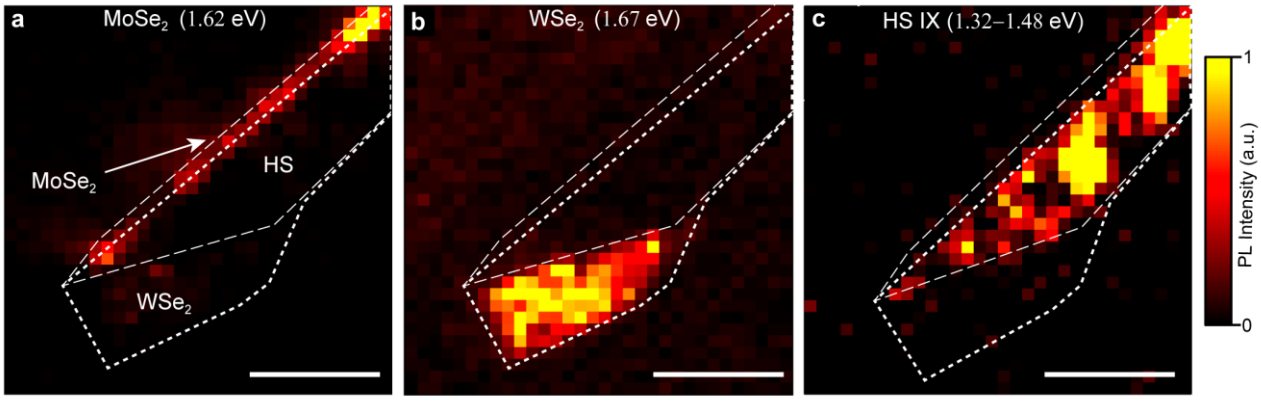

Supplementary Figure S2. Distribution of PL emission. a,b Spatial maps of photoluminescence intensity at 765 nm (1.62 eV), 740 nm (1.67 eV) emission wavelengths, corresponding to MoS_2, WSe_2 intralayer excitonic resonances. Photoluminescence is quenched in the HS area due to efficient charge transfer. c, spatial distribution of interlayer exciton, integrated for 840-940 nm wavelength (1.32-1.48 eV). White dashed lines represent edges of constituent crystals. Scale bar is 5 μm for every panel.

3. Interlayer exciton at high electron densities

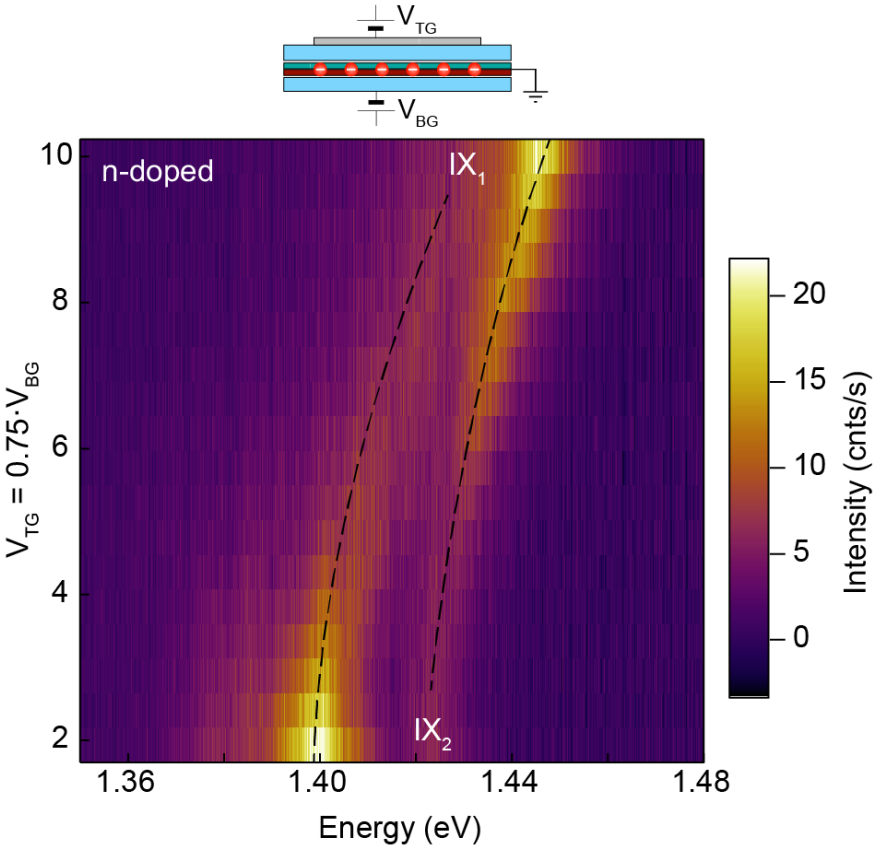

Supplementary Figure S3. Effect of electron concentration on interlayer exciton emission. PL map as a function of the applied voltages to the top and bottom gates in the dual-gate configuration. Here $V_{TG} = 0.75\ V_{BG}$ to minimize the displacement field.

4. Interlayer exciton power dependence

Figure S4 shows the measured dependence of the PL emission intensity on the incident laser power. We note that at low incident powers both peaks show linear power dependency, with no change in their spectral profiles down to 5 nW. At higher power (above 200 µW), the lower energy peak IX_2 shows saturation. Also, both peaks broaden and experience blue shift which we assign to the sample heating and exciton repulsion, respectively. Excitation power higher than 1 mW was not used to avoid potential damage to the sample. We note that while the earliest reports on this type of heterostructures showed saturating PL with power as low as 0.5 µW[1], in recent reports of encapsulated $WSe_2/MoSe_2$ higher values are reported, as in ref.[2] The enhanced efficiency could be related to the reduced linewidth, indication of clean and homogeneous interfaces.

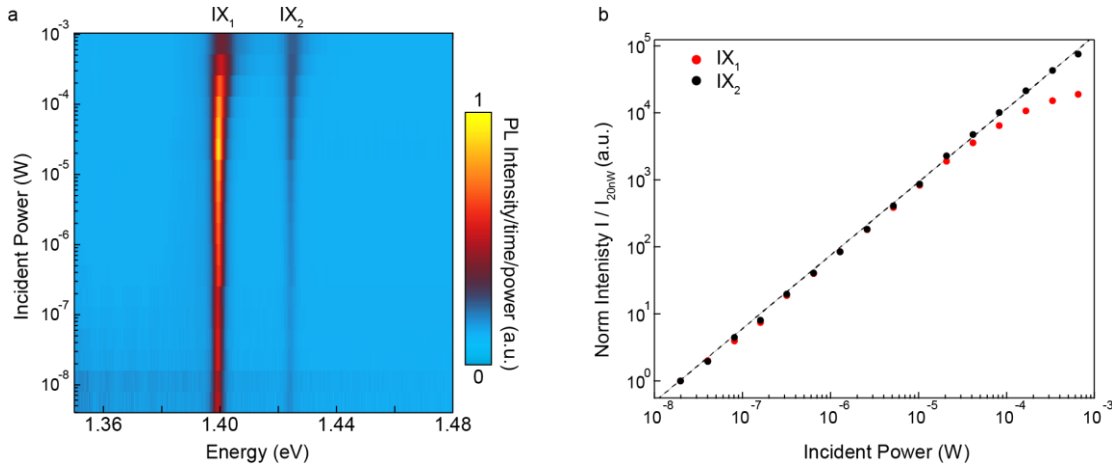

Supplementary Figure S4. Excitation power effect on interlayer exciton emission. a, Power dependency of the PL spectra intensity normalized by acquisition time and incident power. **b,** Emission intensity of IX_1 (red) and IX_2 (black) as a function of the excitation power of the 647 nm laser used. The normalized intensity is the number of counts per second normalized by the emission intensity at 20 nW excitation power.

5. Temperature dependence

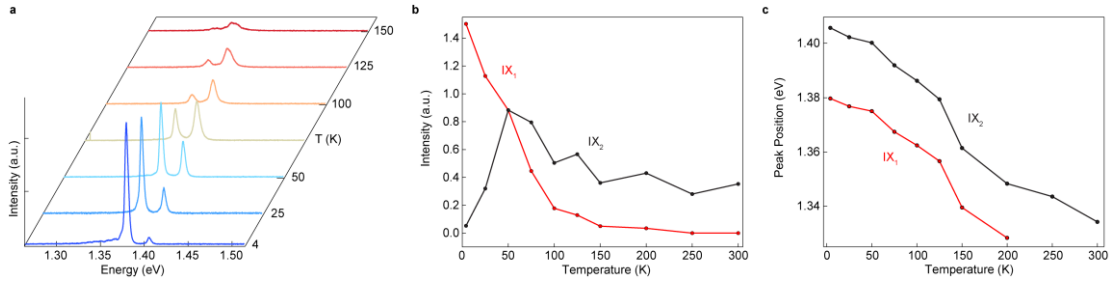

Supplementary Figure S5. Temperature dependence of interlayer exciton emission. a, Interlayer exciton emission spectra as a function of temperature. Plot of the emission intensity (**b**) and energy (**c**) of IX_1 (red) and IX_2 (black) for different temperatures.

6. PL spectra as a function of gating

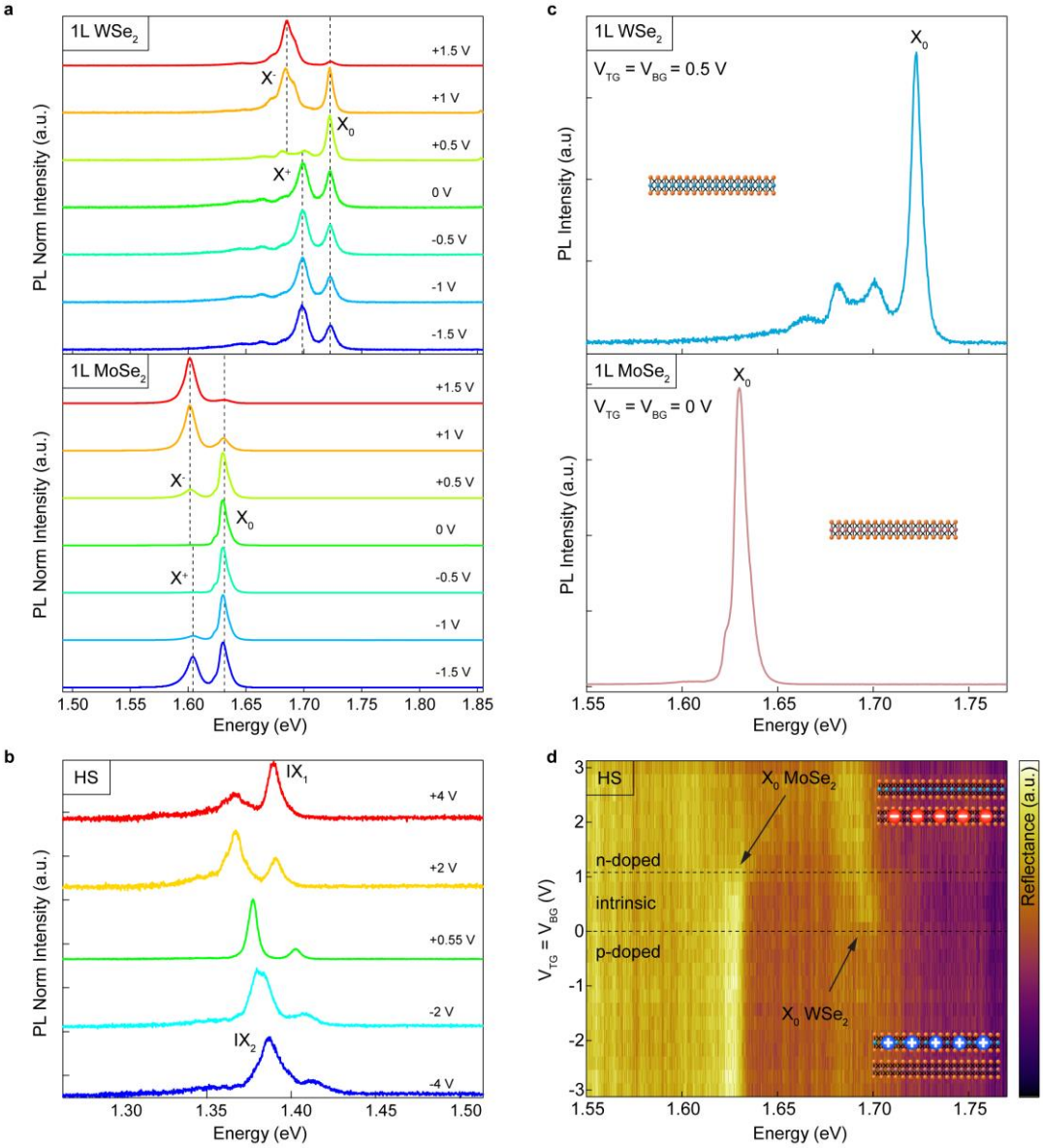

Supplementary Figure S6. Effect of gating on the device optical properties. Gate dependency of the PL spectra acquired on WSe_2 and $MoSe_2$ monolayers (a), and on heterostructure (b). **c**, lowest charge carrier concentration reveals strongest neutral exciton emission in WSe_2 and $MoSe_2$ monolayers. **d**, gate dependency map of reflection spectra from the heterobilayer region. P-doped (n-doped) sample shows only the reflection feature associated to the neutral exciton of $MoSe_2$ (WSe_2), while intrinsic region demonstrates both. This is the direct consequence of the charge transfer associated with type-II band alignment. All measurements are done on the second device, symmetrical dual-gating is used: $V_{\mathrm{BG}} = V_{\mathrm{TG}}$.

7. Additional spectra from inter- and intra-layer excitons as a function of gating

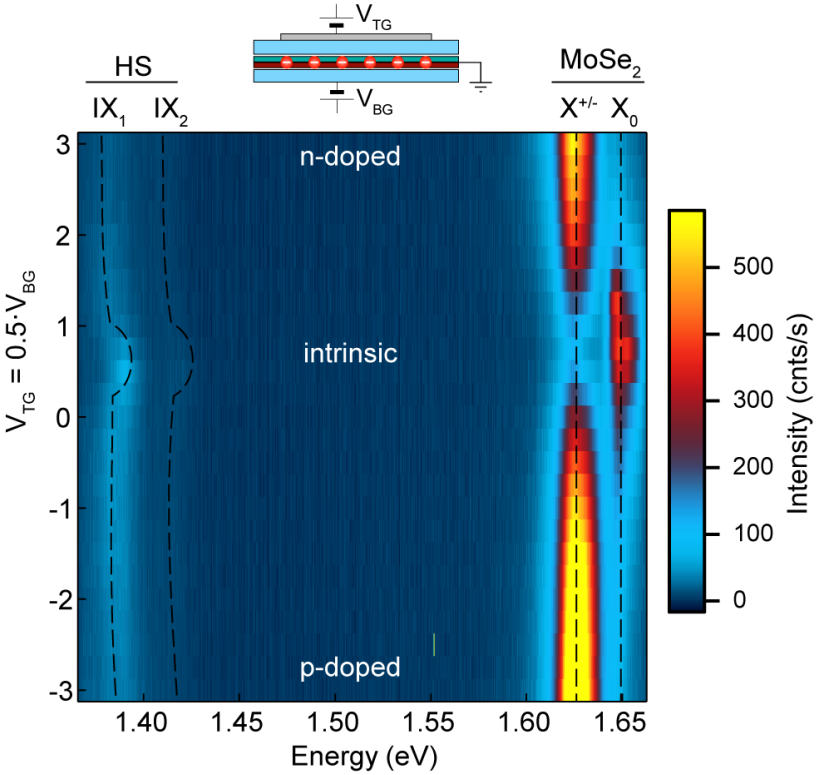

Supplementary Figure S7. Direct comparison of inter- and intra-layer excitonic emission spectra. PL spectra acquired on the edge of heterostructure, showing emission of both intralayer exciton of $MoSe_2$ and interlayer doublet. High-energy, high-intensity interlayer emission appears at the same carrier concentration as neutral exciton of $MoSe_2$, denoted as intrinsic region.

8. Polarization-resolved spectra from individual monolayers

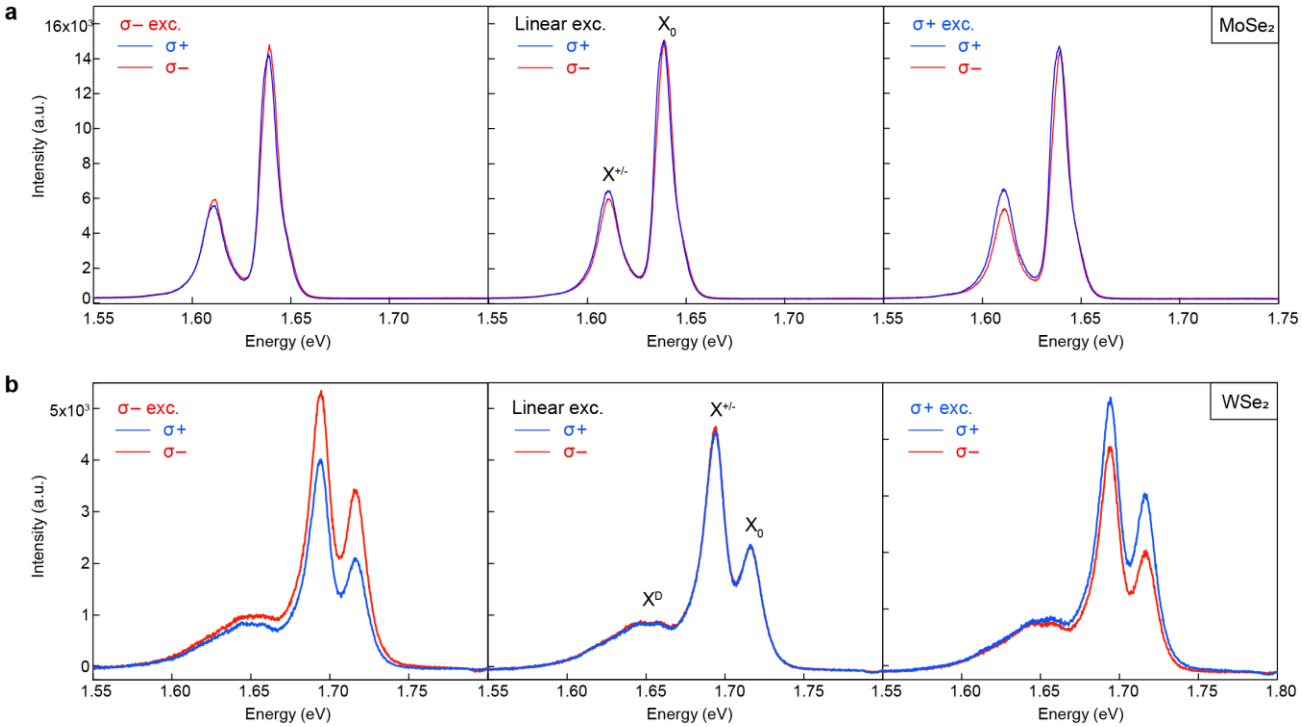

Supplementary Figure S8. Polarization-resolved PL from monolayer $MoSe_2$ and WSe_2. PL spectra showing left- and right-circularly polarized emission components (red and blue respectively) for the case of linear, left- and right-polarized excitation in monolayer $MoSe_2$ (a) and WSe_2 (b).

9. Polarization-resolved spectra from the heterostructure

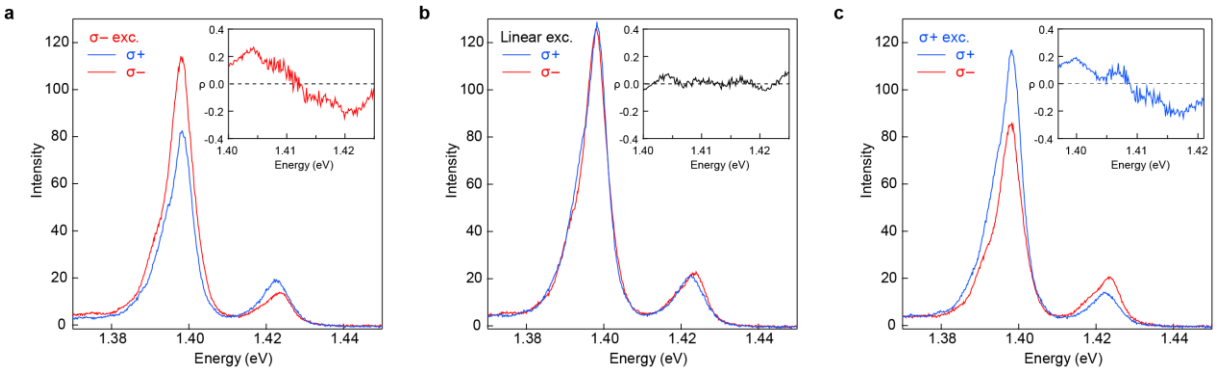

Supplementary Figure S9. Polarization-resolved PL from the $WSe_2/MoSe_2$ heterobilayer. μ-PL spectra for left and right emission from the heterobilayer in the case of **a,** left-circularly-polarized excitation. **b,** linear excitation and **c,** right-circularly-polarized excitation). Insets show the calculated polarization degree $\rho = \frac{I(\sigma^+)-I(\sigma^-)}{I(\sigma^+)+I(\sigma^-)}$. We note that the use of excitation wavelength at resonance with the monolayer excitonic peaks could increase this figure considerably.

10. Polarization-resolved spectral maps

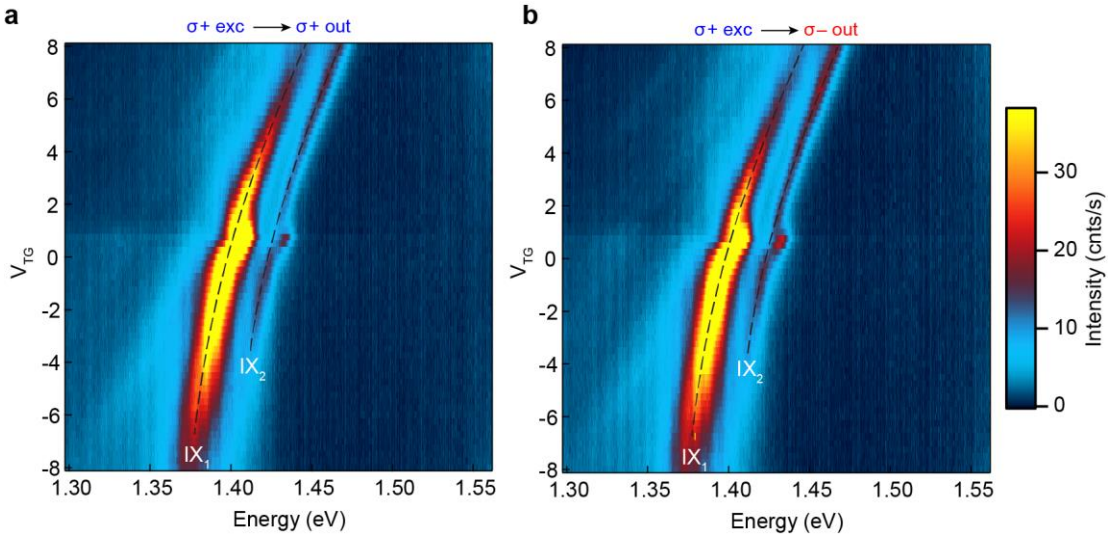

Supplementary Figure S10. Polarization-resolved PL map. PL spectra showing right (a) and left (b) circularly polarized emission components as a function of applied top-gate voltage, when heterostructure is pumped with right-circularly-polarized light.

11. Characterization of the second device

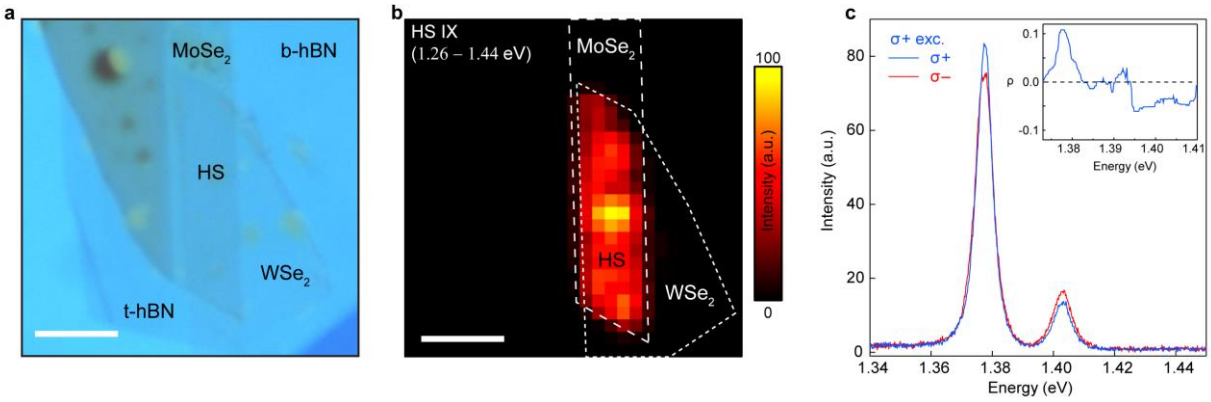

Supplementary Figure S11. Characterization of the second device. a, optical image of the heterc spatial map of the photoluminescence emission integrated between 1.26 eV and 1.44 eV that corres interlayer exciton. Dashes lines indicate edges of the constituent layers. Scale bar is 5 μm for **a** and **b**. **c,** resolved μ-PL spectra for right and left emission from the heterobilayer in the case of right-circula excitation. The inset shows the calculated polarization degree $\rho = \frac{I(\sigma^+)-I(\sigma^-)}{I(\sigma^+)+I(\sigma^-)}$.

12. Discussion of proposed mechanisms for double interlayer transition

Our results can be explained in the frames of several recently proposed theoretical models. In the following we examine them, and compare them with our experimental data.

Given the energy difference between IX_1 and IX_2 of 25 meV, it is natural to interpret the doublet feature as a result of the spin splitting in the conduction band (CB) of $MoSe_2$[3] (roughly one order of magnitude smaller than the WSe_2 valence band (VB) splitting). A very recent work interpreted IX_1 and IX_2 as the result of a transition between VBM in WSe_2 at K/K´ points and CBM in $MoSe_2$ at Q/Q´ points with relaxed selection rules[2]. The presence of polarization-reversing transitions can then be explained

by considering the relaxed selection rules in the case of indirect interlayer excitons. Indeed, DFT calculations of the matrix elements for recombination between spin-orbit- split conduction band at the Q point and valence band at the K point yield similar weights and opposite helicities[2]. Similarly, the temperature and power dependence we observe are in principle compatible with this picture. Concerning the switching between positive and negative polarization observed for IX_1, this may arise from a shift between a Q-K transition to a different one (K-K or K-Γ) because of doping. Calculations for the band structure of two-dimensional materials indeed showed that large shifts and even crossings are possible at high doping levels[4–6]. However, our observation of the sharp switching and the small doping required to trigger the effect do not match well with this picture. Moreover, the strong quenching of interlayer emission as a function of temperature (and stacking angle[7]) seems to exclude phonon-assisted indirect transitions as the main channel for IX radiative emission.

Miller et al[8]. proposed that the long-lived IXs in $MoSe_2/WSe_2$ heterostructures involve two different transitions, one being direct in momentum space and the other being indirect. From our results, we exclude that this could be related to IX_1 and IX_2, since the transition probability for a direct or phonon-assisted transition should differ by orders of magnitude. The temperature dependence would contradict our observations of IX_1 and IX_2 having similar intensities. Also, the strength of the transition suggests well-aligned layers[7], for which the K-K dipole momentum is much stronger.

A likely explanation for the multiple emission lines and their behaviour could come from taking into account the lattice mismatch between $MoSe_2$ and WSe_2 that results in the formation of a moiré pattern. In this work, we consider two different approaches to moiré, namely the one proposed by Yu et al.[9,10] and the one in ref.[11,12]. Due to the spatially-changing stacking order, a periodic array of different symmetry points is produced, with different selection rules from site to site. Even in a well-aligned ($\delta\theta \lesssim 1°$) $WSe_2/MoSe_2$ heterobilayer, the small difference in the lattice constant for the two crystals[13] $\delta = \frac{|a-a'|}{a}$ will produce a moiré pattern with a period $\lambda_M \sim \frac{a}{\sqrt{\delta^2+\delta\theta^2}}$ of a few tens of nanometres. This means that our optical measurements (spot size ~1 μm) probe the behaviour of tens to hundreds of different stacking sites.

In the main text, we discuss how the prediction of a brightened triplet transition can fit our data well. We now explain this in further detail. As calculated in ref.[10], the exciton energy minima corresponds with regions of the moiré pattern with the local R^X_h atomic registry. Here, both spin-conserving (IX_1) and spin-flipping transitions (IX_2) are allowed. They couple to opposite circular polarizations of light, with comparable transition dipole strengths (see Figure S12). These two optical transitions, coming from sites with the same local registry, are expected to show a similar Stark shift in the electric field, which is in agreement with our observations (Figure 2a from the main text). We rule out the possibility that we observe emission from different moiré sites since they would be associated with different dipole strengths due to variations of interlayer distance within the moiré and thus exhibit significantly different slopes of the Stark effect (and potentially crossing, as in ref.[9]). A different type of local minima, with

R^h_h registry shows an opposite coupling with polarized light for IX_1, and a coupling with linearly polarized light for IX_2. This picture matches our data remarkably well: with doping, we alter the moiré potential landscape (by filling some minima or by shifting their energy electrostatically), thus localizing the excitons in sites with a different local symmetry. This is accompanied by a change in the coupling with light for IX_1 (sign change in ρ), and in the loss of polarization for IX_2 in the circular basis (ρ becomes zero as it is now coupled with linearly polarized light).

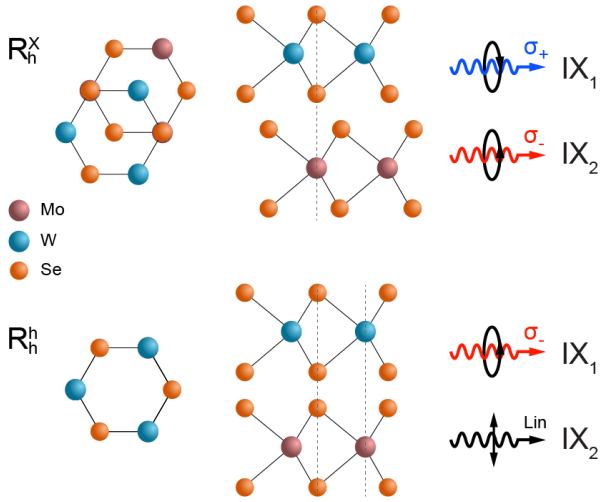

Supplementary Figure S12. Atomic registries in the moiré pattern. Graphical representation of the two different local geometries for R-stacked WSe_2 and $MoSe_2$: R^h_h and R^X_h, (top- and side-view), together with the predicted coupling with light for IX_1 and IX_2 according to ref.[10].

Other studies[11,12] have explained the doublet feature in terms of ground- and excited states of interlayer excitons localized in the moiré potential, where the splitting would result from the moiré potential well. These calculations show multiple transitions with alternating selection rules, with a predicted optical absorption peaks separated by ~10 meV. The same authors also report the observation of 4 peaks with opposite polarizations. It is interesting to note that in their case an increase in temperature strongly quenches the high-energy peaks. This alternative moiré-based model cannot be excluded, but the opposite temperature dependence and the reproducible transition doublet we observe suggest a different mechanism in our case.

13. Zeeman splitting in magnetic field

Following the discussion from the previous part we now consider an R-type $WSe_2/MoSe_2$ heterostructure in an external magnetic field. Supplementary Figure S13 schematically depicts how an applied magnetic field *B* lifts the valley degeneracy of the optical transitions between the valence band of WSe_2 and the spin-split conduction band of $MoSe_2$. The simplified model we describe here accounts for the three main contributions to the interaction with magnetic field: spin, orbital and valley.

Spin-Zeeman shift (Δ_s, black arrows in Figure S13) arises due to the interaction of the field *B* with the magnetic moment of the spin, and is proportional to the g-factor of the electron g_s and its spin s_z,

as $\Delta_s = g_s s_z \mu_B B$ which is roughly equal to the μ_BB, where μ_B is the Bohr magneton. The low-energy IX_1 interlayer exciton corresponds to the spin-singlet transition between the conduction and valence bands with the same spin. Therefore, the spin Zeeman effect does not affect IX_1 resonance in any of the valleys, as its effect on the initial and final states is equal and thus the total contribution is zero. In contrast, the higher-energy spin-triplet IX_2 exciton corresponds to the transition between bands with opposite spins (forbidden in monolayers but brightened in the moiré potential), and therefore gets a non-zero spin contribution to the Zeeman splitting of $-4\mu_B$B.

Atomic orbitals contribute only to the Zeeman shift of the valence band, since it has an orbital magnetic moment $m_l = 2\mu_B$, while the conduction band carries zero orbital moment. We represent this component Δ_l to the Zeeman shift with green arrows in Figure S13. Consequently, the orbital part of the field-induced splitting of the transitions in K/-K valleys ($\Delta E = E_K - E_{-K}$) amounts to $-4\mu_B$B. For the optical transition in monolayer TMDCs, this is the only component that plays a significant role, and consequently a g-factor of -4 is typically observed in these systems[14,15].

The valley contribution to the Zeeman shift (Δ_v, blue arrows) is due to the interaction between the magnetic field and the valley magnetic momentum $\tau_z \alpha^{c,v} \mu_B$ of the self-rotating Bloch wavepackets, where $\tau_z = \pm 1$ is the valley index for $\pm$K valley, and $\alpha^c = m_0/m_e^* \approx 1.8$ ($\alpha^v = m_0/m_h^* \approx 2.8$) takes into account the different effective mass of electrons (holes) in the conduction (valence) band of $MoSe_2$ (WSe_2). Here we use $m_e^* = 0.57m_0$ and $m_h^* = 0.36m_0$, as calculated by Kormányos et al[16]. We note that the use of different values from the literature could affect the final numerical result but does not change the general picture. The non-equivalent effective masses of electrons and holes give an additional term $\mp(\Delta_v^h - \Delta_v^e)$ in the $\pm$K valley. In our case, the valley splitting of both IX_1 and IX_2 acquires an additional term of $-2(\Delta_v^h - \Delta_v^e)$. This valley-dependent term can indeed be substantial, as in recent reports of a large g-factor in AB-type stacked $WSe_2/MoSe_2$[17].

Adding up all the components, the total valley splitting induced by the magnetic field $\Delta E = E_K - E_{-K}$ is expected to be $\sim -6\mu_B B$ ($\sim -10\mu_B B$) for IX_1 (IX_2). However, since the IX_2 transition is associated with light of opposite helicity with respect to IX_1, the observed PL peak splitting has an opposite sign: $\Delta E = E_{\sigma+} - E_{\sigma-} = -(E_K - E_{-K}) \approx 10\mu_B B$. This is in agreement with the experimentally observed opposite g-factors of -8.5 ± 1.5 for IX_1 and 7.1 ± 1.6 for IX_2 moiré excitons. We note that the estimation of the shift for IX_2 is less precise than what we get for IX_1, due to the reduced emission intensity, which reduces the signal-to-noise ratio.

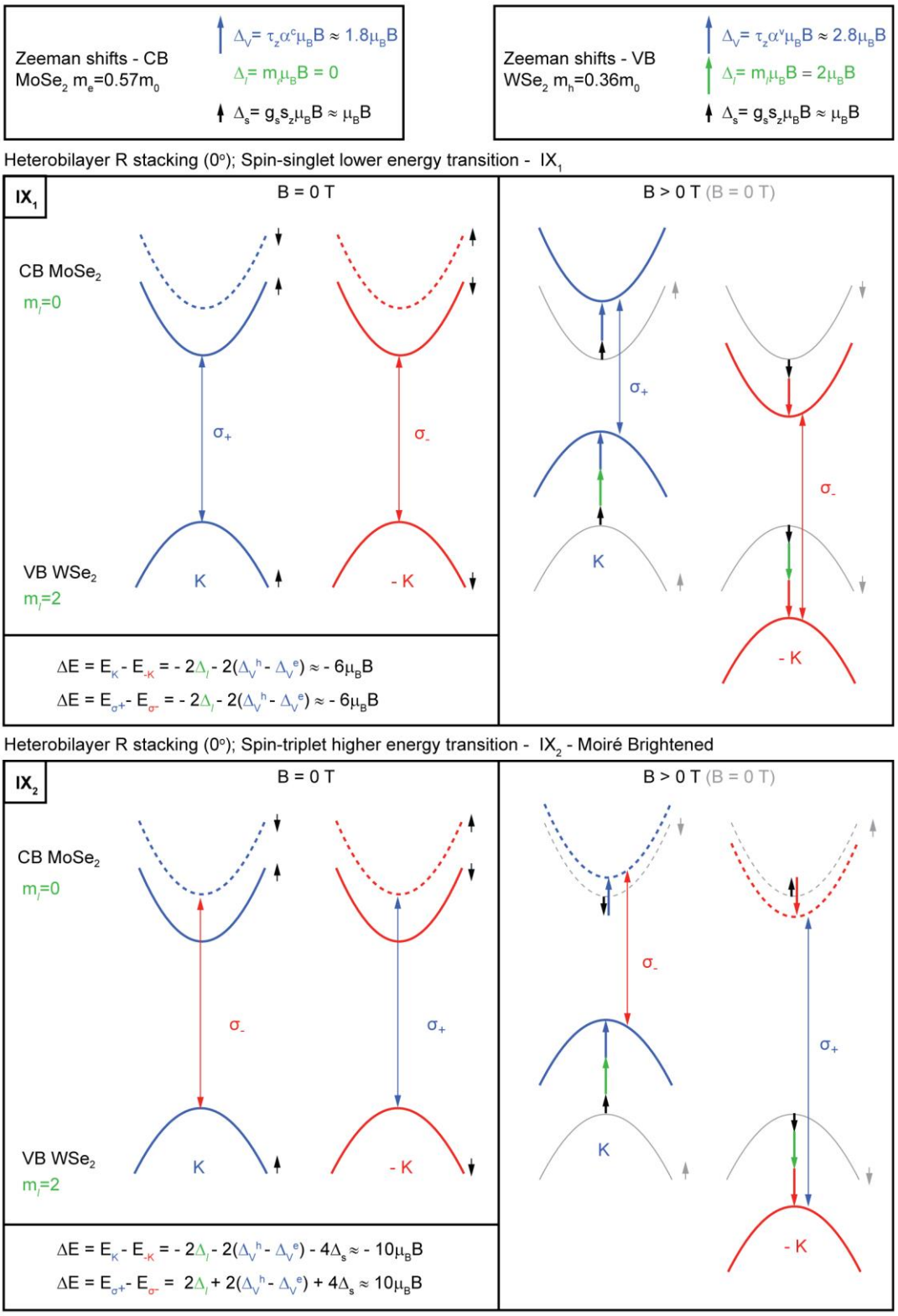

Supplementary Figure S13. Effect of magnetic field on optical transitions. Top panels: spin- (black), orbital- (green) and valley- (blue/red) magnetic moment contributions to the total Zeeman shift. Middle panel: spin-conserving transitions between conduction band of $MoSe_2$ and valence band of WSe_2 in absence (left) and presence (right) of a magnetic field, yielding an effective g-factor of -6. Bottom panel: higher energy transition between conduction band of $MoSe_2$ and valance band of WSe_2 with opposite spins in absence (left) and presence (right) of a magnetic field, yielding an effective g-factor of +10.

SUPPLEMENTARY NOTES REFERENCES

(1) Rivera, P.; Schaibley, J. R.; Jones, A. M.; Ross, J. S.; Wu, S.; Aivazian, G.; Klement, P.; Seyler, K.; Clark, G.; Ghimire, N. J.; et al. Observation of Long-Lived Interlayer Excitons in Monolayer $MoSe_2$–WSe_2 Heterostructures. *Nat. Commun.* **2015**, *6*, 6242.

(2) Hanbicki, A. T.; Chuang, H.-J.; Rosenberger, M. R.; Hellberg, C. S.; Sivaram, S. V.; McCreary, K. M.; Mazin, I. I.; Jonker, B. T. Double Indirect Interlayer Exciton in a $MoSe_2$/WSe_2 van Der Waals Heterostructure. *ACS Nano* **2018**, *12* (5), 4719–4726.

(3) Kormányos, A.; Zólyomi, V.; Drummond, N. D.; Burkard, G. Spin-Orbit Coupling, Quantum Dots, and Qubits in Monolayer Transition Metal Dichalcogenides. *Phys. Rev. X* **2014**, *4* (1), 011034.

(4) Brumme, T.; Calandra, M.; Mauri, F. First-Principles Theory of Field-Effect Doping in Transition-Metal Dichalcogenides: Structural Properties, Electronic Structure, Hall Coefficient, and Electrical Conductivity. *Phys. Rev. B* **2015**, *91* (15), 155436.

(5) Huang, D.; Kaxiras, E. Electric Field Tuning of Band Offsets in Transition Metal Dichalcogenides. *Phys. Rev. B* **2016**, *94* (24), 241303.

(6) Chaves, A.; Azadani, J. G.; Özçelik, V. O.; Grassi, R.; Low, T. Electrical Control of Inter-Layer Excitons in van Der Waals Heterostructures. *ArXiv170908315 Cond-Mat* **2017**.

(7) Nayak, P. K.; Horbatenko, Y.; Ahn, S.; Kim, G.; Lee, J.-U.; Ma, K. Y.; Jang, A.-R.; Lim, H.; Kim, D.; Ryu, S.; et al. Probing Evolution of Twist-Angle-Dependent Interlayer Excitons in $MoSe_2$/WSe_2 van Der Waals Heterostructures. *ACS Nano* **2017**, *11* (4), 4041–4050.

(8) Miller, B.; Steinhoff, A.; Pano, B.; Klein, J.; Jahnke, F.; Holleitner, A.; Wurstbauer, U. Long-Lived Direct and Indirect Interlayer Excitons in van Der Waals Heterostructures. *Nano Lett.* **2017**, *17* (9), 5229–5237.

(9) Yu, H.; Liu, G.-B.; Tang, J.; Xu, X.; Yao, W. Moiré Excitons: From Programmable Quantum Emitter Arrays to Spin-Orbit–Coupled Artificial Lattices. *Sci. Adv.* **2017**, *3* (11), e1701696.

(10) Yu, H.; Liu, G.-B.; Yao, W. Brightened Spin-Triplet Interlayer Excitons and Optical Selection Rules in van Der Waals Heterobilayers. *2D Mater.* **2018**, *5* (3), 035021.

(11) Wu, F.; Lovorn, T.; MacDonald, A. H. Theory of Optical Absorption by Interlayer Excitons in Transition Metal Dichalcogenide Heterobilayers. *Phys. Rev. B* **2018**, *97* (3), 035306.

(12) Tran, K.; Moody, G.; Wu, F.; Lu, X.; Choi, J.; Singh, A.; Embley, J.; Zepeda, A.; Campbell, M.; Kim, K.; et al. Moir\'e Excitons in Van Der Waals Heterostructures. *ArXiv180703771 Cond-Mat* **2018**.

(13) Huang, C.; Wu, S.; Sanchez, A. M.; Peters, J. J. P.; Beanland, R.; Ross, J. S.; Rivera, P.; Yao, W.; Cobden, D. H.; Xu, X. Lateral Heterojunctions within Monolayer $MoSe_2$–WSe_2 Semiconductors. *Nat. Mater.* **2014**, *13* (12), 1096–1101.

(14) Aivazian, G.; Gong, Z.; Jones, A. M.; Chu, R.-L.; Yan, J.; Mandrus, D. G.; Zhang, C.; Cobden, D.; Yao, W.; Xu, X. Magnetic Control of Valley Pseudospin in Monolayer WSe_2. *Nat. Phys.* **2015**, *11* (2), 148–152.

(15) Srivastava, A.; Sidler, M.; Allain, A. V.; Lembke, D. S.; Kis, A.; Imamŏglu, A. Valley Zeeman Effect in Elementary Optical Excitations of Monolayer WSe_2. *Nat. Phys.* **2015**, *11* (2), 141–147.

(16) Kormányos, A.; Burkard, G.; Gmitra, M.; Fabian, J.; Zólyomi, V.; Drummond, N. D.; Vladimir Fal'ko. K · p Theory for Two-Dimensional Transition Metal Dichalcogenide Semiconductors. *2D Mater.* **2015**, *2* (2), 022001.

(17) Nagler, P.; Ballottin, M. V.; Mitioglu, A. A.; Mooshammer, F.; Paradiso, N.; Strunk, C.; Huber, R.; Chernikov, A.; Christianen, P. C. M.; Schüller, C.; et al. Giant Magnetic Splitting Inducing Near-Unity Valley Polarization in van Der Waals Heterostructures. *Nat. Commun.* **2017**, *8* (1), 1551.